Roughness metrics of prismatic facets of ice

S.P. Neshyba[1], B. Lowen[1], M. Benning[1], A. Lawson[1], and P.M. Rowe[2]

[1]University of Puget Sound, Tacoma, WA
[2]University of Idaho, Moscow, ID

Corresponding author's address:
Steven Neshyba
University of Puget Sound Chemistry Department, CMB 1015
1500 N. Warner
Tacoma, WA 98416

[Submitted to the Journal of Geophysical Research – Atmospheres, October 2012]
[Resubmitted February 2013]
[Resubmitted March 2013]

Abstract: We define a surface normal roughness metric for mesoscopically rough ice facets, and present methods for inferring its value from variable pressure scanning electron micrographs. The methods rely on the anisotropic morphology of roughening in the prismatic plane, in which nearly all the variation in surface height occurs in the direction of the main symmetry axis of hexagonal-habit ice prisms. Because of this symmetry, roughening appears at boundaries between prismatic facets in a way that readily permits quantitative analysis. Prismatic surfaces of four ice crystals grown between -45 and -30°C are found to have mean surface normal roughness values of 0.04-0.1, a range that corresponds to Cox-Munk roughness scale parameters 0.3-0.5. The distribution of tilt angles also suggests a Weibull shape parameter smaller than unity, a result that compares favorably with field observations. Shortwave scattering calculations of hexagonal polyhedra with surface morphologies derived from these observations indicate substantial retention of the well-known 22° halo, despite a large (4-6%) reduction in the asymmetry parameter compared to smooth-surface counterparts. We argue that this signature is a generic outcome of the symmetry of the roughening, which in turn originates in the anisotropic surface self-diffusivity of these facets.

1. Introduction

It is widely recognized that ice crystal habit and size are important determiners of the single-scattering radiative properties of atmospheric ice crystals [*Macke et al.*, 1996, 1998; *Gayet et al.*, 1997; *Baran et al.*, 2001; *Bailey and Hallett*, 2004, 2009; *Baum et al.*, 2005a, 2005b; *Heymsfield et al.*, 2006; *Garrett*, 2008; *Baran*, 2009, 2012]. Because cirrus and contrail cirrus are ice-containing clouds that modulate the radiative properties of the atmosphere in significant ways, considerable research has been aimed at constructing climatologies of ice particle size and shape relevant to general circulation models and remote sensing [*Cox*, 1971; *Crane and Barry*, 1984; *Stephens et al.*, 1990; *Yang et al.*, 2005; *Edwards et al.*, 2007; *Bourdages et al.*, 2009; *Baran*, 2012].

Compared to ice crystal size and shape, there have been fewer investigations into how mesoscopic (micrometer-scale) surface roughness affects an ice crystal's single-scattering radiative properties. The motivation for seeking such an effect stems from a combination of observations. Hexagonal ice columns are known to be common in cirrus clouds, and frequently occur as parts of more complex ice crystals [*Heymsfield and Platt*, 1984]. It has long been known that cirrus particles can fall through sub-saturated air for several kilometers before sublimation is complete (approximately one third of the vertical extent of cirrus clouds has been identified as a "sublimation zone"), that sublimation roughens ice surfaces on a mesoscopic scale, and that such roughening can have discernable radiative consequences [*Cross*, 1969; *Davy and Branton*, 1970; *Heymsfield and Donner*, 1990; *Lynch*, 2002]. Discrepancies between observed asymmetry parameters of ice crystals comprising ice clouds and expected values based on smooth ice surfaces have led

several investigators to postulate roughness as a possible cause [*Garrett*, 2008; *Baran*, 2009, and references therein].

Much of what is understood about the radiative effects of mesoscopic roughening derives from modeling studies. Single-scattering ray-tracing studies have used random-tilt algorithms, in which hexagonal prisms (and more complex habits) are "distorted" or "roughened" in the sense that rays of light passing through the ice-air interface are redirected in some way [*Macke et al.*, 1996; *Yang et al.*, 2008a, 2008b]. These phenomena have led several authors to the conclusion that roughening, should it occur, would have measureable effects for remote sensing and climate modeling. When remote sensing retrieval algorithms at visible and near-infrared wavelengths include roughness, for example, retrieved optical thickness is significantly reduced [*Yang et al.*, 2008b; *Xie*, 2012]. In a study of electronically levitated ice-analog crystals, [*Ulanowski et al.*, 2006] have argued that it may be possible to use scattering patterns to obtain surface information of ice crystals. Direct observational evidence of mesoscopic roughness on atmospheric ice crystals is comparatively sparse, however, because aircraft-deployed imaging instruments, while extremely useful for characterizing habit and projected surface area, usually cannot resolve mesoscopic surface roughness [*Schmitt and Heymsfield*, 2007]. Direct in situ evidence has been reported only in rare cases: photographs of atmospheric ice crystals collected on the ground at South Pole Station [*Walden et al.*, 2003], for example, are suggestive of trans-prismatic roughening on the exterior prismatic surfaces of hexagonal crystals. Surface roughness on atmospheric ice has also been inferred from a combination of nephelometry and cloud particle imaging

[*Shcherbakov et al.*, 2006a, 2006b].

In the laboratory, [*Sazaki et al.*, 2010] have presented confocal microscopy images of faceted ice surfaces that indicate monolayers extending tens of micrometers across a facet, and [*Cross*, 1969] has presented scanning electron microscopy micrographs of ablating bulk ice that indicated roughness over a range of mesoscopic scales. Recently, [*Pfalzgraff et al.*, 2010] have presented scanning electron microscope (SEM) micrographs of substrate-grown hexagonal ice prisms, in which roughening was promoted by mild supersaturation and subsaturation conditions. Advantages of variable pressure scanning electron microscopy (VPSEM) include high resolution and the ability to finely tune vapor pressure and temperature within the SEM chamber, capabilities that permit examination of ice crystal response to multiple growth and ablation cycles. Challenges include linking ice processes occurring in a VPSEM chamber to those in the atmosphere, since VPSEM-grown crystals reported to date are attached to a substrate, and are surrounded by gas at only 50-200 Pa pressure, whereas cirrus ice grows unattached at pressures typically 20 kPa [*Harrington et al.*, 2009]. Neither limitation is a permanent feature of VPSEM however. Improvements in VPSEM technology have already made imaging possible at pressures of several thousand pascals [*Mathieu et al.*, 2007], and techniques for growing ice crystals without a substrate can, in principle, be implemented within a VPSEM [*Bacon et al.*, 2003]. The potential of VPSEM for laboratory studies relevant to cirrus ice crystals therefore seems promising.

To exploit this technology in a way that allows one to make climatologically relevant

statements about the radiative effects of ice mesoscopic roughening, a number of practical questions need to be addressed. One set of questions has to do with identifying statistically meaningful properties ("metrics") that are most relevant to atmospheric radiative transfer and remote sensing. Is it more important to describe the depth of roughening, or its spatial wavelength? How important is surface anisotropy? A second question concerns the methodology of inferring values of these metrics from VPSEM micrographs: *how* does one infer three-dimensional roughness from two-dimensional images? Such questions can be addressed at present, in the context of presently available VPSEM technology, in anticipation of more sophisticated experimental technologies for studying ice that will eventually become available.

In this paper, we describe our experimental procedure for growing and manipulating ice crystals in a VPSEM chamber so that the resulting micrographs are suitable for roughness analysis. In section 3 we describe two methods for inferring surface height functions from VPSEM micrographs obtained as part of this work. One method is appropriate for circumstances in which the roughening is deep compared to instrument resolution. A second method is developed for circumstances in which roughening is apparent, but is shallow compared to instrument resolution. We also define a roughness variable, the spatial average and probability distribution of which are the main metrics of interest. In section 4 we present the results of ray-tracing calculations based on hexagonal polyhedra whose prismatic facets have been roughened in accordance with surface height functions derived from these VPSEM micrographs. In section 5 we discuss our results in the context of other work.

2. Methods

2.1 Experimental

Micrographs were taken using a Hitachi S-3400N variable pressure scanning electron microscope (VPSEM) equipped with a backscattered electron detector, using a protocol described by [*Pfalzgraff et al.*, 2010]. Typical operating conditions used an accelerating voltage of 12 kV and a probe current of 90, with all four central detectors (A, B, C, D). In a typical experiment, a rough-cut copper specimen stub was mounted on an examination stage atop a Deben Ultra-Cool stage MK3 version Peltier cooling element set to room temperature. An aluminum reservoir containing 4 mL of de-ionized ice initially at -15°C was placed in the VPSEM chamber, the chamber closed and pumped down to a nominal operating pressure of 50 Pa. Upon reaching that pressure, the Peltier cooling system was set to -45°C. The examination stage was then monitored at low magnification (20×) until the first ice crystals appeared, typically only a few minutes. Subsequent manipulations involved raising and lowering the temperature of the Peltier cooler over the range -45°C to -30°C.

The geometry of the Hitachi S-3400N VPSEM is such that the electron beam source passes through four backscattered electron detectors positioned symmetrically around the beam. Since electron backscatter signals received at the four detectors are combined with equal weight in forming micrographs, their midpoint is centered on the path of the electron beam. The vector defined by beam electrons moving toward the sample, therefore, is antiparallel to the vector defined by backscattered electrons moving back to the detector midpoint. In this paper, we will refer to the latter as the normalized viewing

vector, $\vec{d}$. Figure 1 shows a sinusoidal surface height function, $y(z)$, with the viewing vector and surface orthogonal, $\vec{n}$, for reference.

2.2 Definition of a roughening metric

In this paper, we use the term "mesoscopically rough" to connote a condition of variable surface morphology on scale of 1-20 μm. We use the term "roughness variable" to indicate a local measure of surface morphology, e.g., the tilt angle at a given point on a surface. The term "roughness metric" indicates a statistical property of such variables, e.g., the mean tilt angle over some surface region. Roughness metrics encompass the more specific "roughness parameter", which connotes parameters of a given analytical roughness representation, e.g., the width of a distribution of tilt angles.

We seek a quantitative, general-purpose roughness metric relevant to radiative single-scattering that will allow us to compare observed roughness metrics to parameters of different extant roughness representations. To do so, we begin with the projection of a normalized surface orthogonal, $\vec{n}$, onto the viewing vector, $\vec{d}$,

$$\mu\,(z) = \vec{n} \cdot \vec{d} = cos\phi \tag{1}$$

where ϕ measures the angle between these two vectors; it is also equal to the angle subtended by the local tilt angle, i.e., the tangent to the surface at location z with respect to a reference plane,

$$tan\phi = dy/dz. \tag{2}$$

The variable μ is closely tied to the local reflectivity of a surface: if $\mu = 1$, the surface faces the viewer in a way that strongly favors reflection of electron density (or in other circumstances, light). Smaller values of μ mean the surface is inclined away from the viewing vector, resulting in less reflection back toward the viewer. It is convenient to define a complementary parameter to the normal reflection parameter,

$$r \equiv 1 - \mu. \tag{3}$$

Increasing values of r indicate increasing roughness. Therefore, we refer to this quantity as the *surface normal roughness variable.* The spatial average of r, the *mean surface normal roughness* (designated $< r >$) is the roughness metric of primary concern to us here, but of course other metrics, e.g., higher moments of *r*, may also be useful. We can anticipate that $< r > \geq 0$ for any given region of a surface, the equality holding for a smooth surface directly facing the viewer. The value of r at a given point on a surface can be calculated from the local surface tangent. Using Eqs. (1-3) in combination with the identity $\cos(\arctan(a)) = \left(\frac{1}{1+a^2}\right)^{1/2}$, we obtain

$$r = 1 - \left(\frac{1}{1+\left(\frac{dy}{dz}\right)^2}\right)^{1/2} \tag{4}$$

Equations (1-4) allow us to compute the mean surface normal roughness for any single-valued surface height function intended to represent surface roughness, whether the representation be observed or analytical. For example, taking a sinusoidal surface height function with spatial wavelength λ shown in Fig. 1,

$$y(z) = A\,cos(\frac{2\pi z}{\lambda}) \tag{5}$$

as a representation of surface roughness, we can identify the *characteristic sinusoidal angle*, δ_c, as a roughness parameter of this representation. This angle is the angle subtended by this height function when the argument of the cosine is $\frac{\pi}{2}$, and is related to the amplitude, A, and spatial wavelength, λ, of the sinusoid by

$$\tan \delta_c = 2\pi A/\lambda. \tag{6}$$

Integrating Eq. (4) over a single wavelength of the sinusoidal function of Eq. (5) leads to

$$< r >= 1 - 2K(tan^2\delta_c)/\pi \tag{7}$$

where K is the elliptic-K function. Equation (7) expresses the mean surface normal roughness metric ($< r >$) as a function of the roughness parameter for a sinusoidal roughness representation (δ_c). A useful approximation for the inverse of Eq. (7) is

$$\delta_c \approx \text{acos}\,(1 - 2 < r >) \equiv \delta_c^{\circ} \tag{8}$$

which is accurate to 3% in the range $0° < \delta_c < 30°$.

Three representations of surface roughness used widely in light-scattering calculations of cirrus ice models are the uniform random-tilt (URT) [*Macke et al.*, 1996], the Cox-Munk random-tilt (CMRT) [*Cox and Munk*, 1954; *Yang and Liou*, 1998], and the Weibull random-tilt (WRT) [*Dodson*, 2006; *Shcherbakov et al.*, 2006b] algorithms. All invoke random, azimuthally isotropic tilt angles in the plane of interest, e.g., basal and prismatic facets of hexagonal polyhedra. URT roughening is parameterized by a maximum roughening angle, ϕ_{max}, which defines the Macke distortion parameter $t_M = \phi_{max}\left(\frac{2}{\pi}\right)$. WRT roughening is parameterized by scale and shape parameters σ_W and η_W. When the Weibull shape parameter equals unity, Weibull statistics coincide with CMRT roughening, i.e., $\sigma_{CM}=\sigma_W$ when $\eta_W=1$ (see Eq. A6 of *Shcherbakov et al.*, 2006 for a closed-form expression). In each case, the distribution of tilt angles implies a distribution in the surface normal roughening variable, r, (Eq. (1)), hence a value of $<r>$. Equating $<r>$ across models as the basis for determining equivalent roughness metrics yields similar values for t_M and σ_{CM}. The foregoing suggests as homologous roughness parameters

$$t_M \approx \sigma_{CM} \approx \delta_c\left(\frac{2}{\pi}\right) \approx \delta_c^{\circ}\left(\frac{2}{\pi}\right) \tag{9}$$

These are displayed as a function of $< r >$ in Fig. 2. Also shown in Fig. 2 are values of $< r >$ obtained from VPSEM experiments, described below.

2.3 Ray tracing methods

In the numerical ray tracing computer code of [*Macke*, 1993; *Macke et al.*, 1996], objects are represented as a set of planar polyhedra, which together form a three-dimensional polyhedron. In the present application, we embed into initially smooth prismatic facets of a hexagonal polyhedron a series of additional planar polyhedra whose orientations are specified by surface height functions obtained from VPSEM micrographs. A smooth 5% margin is specified at basal ends. Ray tracing analysis of these polyhedra typically consisted of 100 rays per crystal orientation, for 10^4 crystal orientations, with a maximum of 20 ray recursions and 200 internal ray reflections permitted, using a shortwave wavelength of 0.5 μm and complex refractive index of $n=(1.313+1.910\times10^{-9}i)$ [*Warren and Brandt*, 2008]. In all calculations described below, energy loss estimates were smaller than 0.01%. Phase functions produced by these calculations were normalized using a Gaussian-fitted forward peak using an algorithm of [*McFarlane and Evans*, 2004]. These normalized phase functions were then analyzed for Legendre moments. Here, we focus on the first Legendre moment, also known as the asymmetry parameter.

3. VPSEM-derived roughness metrics

3.1 Extracting surface height functions from VPSEM micrographs

Figure 3 displays a time series of VPSEM micrographs of a crystal having two intersecting prismatic facets, the edge between them appearing as a bright diagonal line across the figure. The orientation of the crystal is such that the facet on the upper right faces the viewer directly, i.e., the surface normal is parallel to the viewing vector. The other facet, henceforth the "inclined" facet, has a surface normal inclined 60° away from

the view vector. The series of images resulted from manipulations designed to expose corrugations in profile. Once grown (A-B), the crystal was subjected to elevated temperatures, during which time extensive surface ablation occurred on both prismatic surfaces, appearing as trans-prismatic strands, or corrugations (C-E). The temperature of the crystal was then reduced for a time sufficient to restore the normal facet, but not the inclined facet, to a smooth appearance (F-H). The caption to Fig. 3 contains details about the timing associated with these micrographs.

Figure 4 displays micrographs of four crystals grown and imaged according to the methods described previously. The first row reproduces Fig. 3H, hereinafter referred to as Crystal I. To extract a surface height function for Crystal I, we digitized x-z coordinates along the bright prismatic facet boundary in the lower right-hand-side by inspection of the micrograph, applied a rotation to remove the slant, and multiplied by $\sin(60°)$ to convert apparent heights to true heights above the inclined facet. The resulting surface height function, $y(z)$, is displayed in the center column of Fig. 4, along with the surface roughening variable derived from it using Eq. (4). The standard deviation in surface height, σ_y, and the mean surface normal roughening, <r>, are also indicated on these graphs.

Crystal II (second row of Fig. 4) was grown and maintained at -45°C, and imaged about thirty minutes after the crystal first appeared on the cold stage. It was not exposed to ablation (sub-saturation) conditions at any time during its growth. Roughness was deep

enough to permit analysis using the same method as for Crystal I, i.e., by manually digitizing x-z coordinates along the bright prismatic facet boundary.

Crystal III (third row of Fig. 4) was also grown under conditions similar to the early stages of crystal I (Fig. 3, panels 3A-B). The micrograph shows two intersecting prismatic facets, designated "normal" and "inclined" as previously, the boundary between them forming a bright horizontal line. The part of region R that lies above the prismatic facet boundary samples a roughened part of the normal-oriented prismatic facet. Like Crystal II, this crystal was never subjected to ablation conditions, but unlike Crystal II, it developed only shallow roughening; the relief presented at the prismatic facet boundary of this crystal is only slightly greater than the pixel resolution. We can still extract a surface height function, however, using spline-fit backscattered electron intensity profiles in the vicinity of the facet boundary. Figure 5 shows an ensemble of profiles of backscattering intensity, *I(x)*, within region R of Crystal III. Peaks near x=180 μm mark the prismatic facet boundary: intensities to the left correspond to the roughened, normal facet, while intensities to the right correspond to the smooth, inclined facet. Close inspection reveals that bright lines in the rough region tend to meet the prismatic facet boundary at smaller values of x than dark lines. We will refer to these values as $x_{boundary}(z)$. For example, the profile highlighted with circles in Fig. 5 corresponds to a *bright* vertical line at the center of the rough part of R of Crystal III. The profile highlighted with squares corresponds to an adjacent *dark* vertical line. It is evident that the bright line is characterized by a smaller value of $x_{boundary}$ compared to the dark line. This is a repeating pattern. Like a corrugated roof cut at an angle, these properties imply

that the alternating bright and dark vertical lines in the rough region of Crystal III correspond to protrusions and depressions with respect to the plane of the normal facet. Values of $x_{boundary}$ obtained in this way, over a range of z-values, are used to calculate a surface height function with respect to the normal prismatic facet,

$$y(z) = -(x_{boundary}(z) - x_{baseline}(\mathrm{z})) \times \tan(60°) \quad (10)$$

where $x_{baseline}$ accounts for the gradual upward drift in the position of the prismatic facet boundary appearing in region R, and the tangent term converts to true heights above the normal facet plane.

Crystal IV (fourth row of Fig. 4) was grown under conditions similar Crystal III. Although primarily shallow, short segments of the surface suggest microfaceting, i.e., faceting of a micrometer scale.

Roughness metrics and temperatures associated with Crystals I-IV are presented in Table I. Some qualitative conclusions can be drawn from these data. It is evident that prismatic roughening in all four crystals is highly anisotropic: corrugations occur in the trans-prismatic *x*-direction. In addition, it is evident that the roughening in Crystals I and II is deeper (characterized by σ_y>1 μm) than the roughening in Crystals III and IV (σ_y<1 μm). This distinction is not clearly correlated to growth or ablation conditions, however, since the roughness in Crystal I resulted from ablation, whereas the roughness in Crystals II-IV resulted from growth. In general, however, it is clear that a much larger sample size is

needed to establish statistically meaningful correlations between roughness and important atmospheric variables, and indeed whether roughness of this kind will occur at temperatures outside the range studied here (-45 and -30°C).

3.2 Probability density functions of the surface normal roughness variable

Figure 6 compares VPSEM-observed probability density functions of the surface normal roughness variable with random-tilt representations whose parameters have been set to match that of Crystal I. For crystals I and III, it is evident that the distribution in r is more sharply peaked at low r-values compared to URT and CMRT roughness; matching this behavior seems to require Weibull statistics with η_W between 1 and about 0.75. Crystal II exhibits a much lower probability at small r-values than random-tilt representations of similar roughness, and moreover has a prominent peak at r=0.06, which corresponds to a local tilt angle of 20°.

4. Ray tracing results

Polyhedra with VPSEM-derived roughness are displayed in the right-hand column of Fig. 4. They have been assigned an aspect ratio of four, in accordance with field observations at South Pole Station as the most probable value for hexagonal columns in that location [*Walden et al.*, 2003]. Figure 7 shows in gray shades the ray-tracing results for these crystals. Also shown are results for a smooth-surface polyhedron and a polyhedron for which a URT roughening algorithm was applied [*Macke et al.*, 1996]. The latter was parameterized to have a mean surface normal roughness equal to that of Crystal I. Of particular interest are the impacts of roughening on the 22° halo and the 120° minimum,

both prominent features of smooth hexagons. The 120° minimum is suppressed by both URT and VPSEM-derived roughening, although this suppression is more extreme in the latter case. The 22° halo, in contrast, is far more resilient to VPSEM-derived roughening than to URT roughening; it remains quite distinct in all four VPSEM-derived cases presented here. (One quantitative measure of halo brightness is the ratio $P_{11}(23°)/P_{11}(0°)$, which is only 10% smaller in the VPSEM-derived roughening cases compared to smooth counterparts (about $2x10^{-4}$). The Supplement displays more detailed views of the low-angle parts of these functions.) Enhanced resilience of the 22° halo to VPSEM-derived roughening is due, we believe, to the trans-prismatic symmetry and quasi-periodicity of this roughening. In support of this hypothesis, we have found that even sinusoidal trans-prismatic roughening results in substantial retention of the 22° halo (also shown in Fig. 7; the model polyhedron is shown in the Supplement). Figure 7 also shows the linear depolarization ratio for VPSEM-derived and URT roughening, which tells a similar story of resilience of the 22° halo to trans-prismatic roughening.

Asymmetry parameters derived from the VPSEM-derived phase functions described above are shown in Fig. 8, along with smooth-surface and URT-roughened counterparts. The reduction in asymmetry parameter due to VPSEM-derived roughness, relative to smooth-surface counterparts of the same size and aspect ratio, is 4-6%. This reduction is considerably greater than for URT-roughened hexagonal crystals of the same size, aspect ratio, and equivalent roughening parameterization.

5. Discussion

The extent to which the roughening that occurs in our VPSEM experiments can reliably inform us about roughening in natural atmospheric ice is a matter that calls for careful consideration. First, we consider arguments pertaining to mechanisms by which roughening occurs. It has been argued [*Pfalzgraff et al.*, 2009] that roughening mechanisms could be different because cirrus cloud crystals grow unattached to a substrate, in a total ambient pressure of ~200,000 Pa [*Harrington et al.*, 2009], whereas the VPSEM-imaged ice crystals described here are attached to a substrate in a chamber containing mostly water vapor at 50 Pa. The received view of atmospheric ice crystal growth is that it proceeds via step initiation at facet boundaries [*Hobbs and Scott*, 1965; *Gonda et al.*, 1994, 1994; *Nelson and Baker*, 1996; *Jeong and Williams*, 1999]. Since roughness in VPSEM experiments occurs atop facets not in contact with any substrate (as well as facets that are in contact with the substrate), we can expect similar mechanisms to prevail. The question of the effect of ambient (air) pressure must be regarded as open; VPSEM or environmental SEM experiments at higher pressure should be able to resolve this matter.

A second set of considerations concerns field evidence of prismatic roughening. We reproduce in Fig. 9 three high-resolution photographs of fallen ice crystals collected in the field. All were obtained above a snow-covered surface in the absence of falling snow or flurries. Figure 9a was recorded at South Pole Station during the Austral winter [*Walden et al.*, 2003]. Mesoscopic structure of trans-prismatic symmetry is evident as dark, annular lines around partially hollowed hexagonal columns. Figure 9b shows

atmospheric ice crystals collected at Summit, Greenland during the Arctic winter [*Walden*, personal communication]. Trans-prismatic roughening is also evident in this image, in this case plainly on the exterior of prismatic facets. The collection protocol that yielded images such as these was such that accumulation typically occurred over a span of hours. Moreover, such roughening is conspicuously absent from the summertime portion of the Summit dataset, with some exceptions: Figure 9c shows a summertime crystal photographed at Summit, Greenland.

Other field observations provide indirect evidence for roughening in natural atmospheric ice. In a ground-based nephelometry study at South Pole Station, [*Shcherbakov et al.*, 2006b] (henceforth SGBL) present scattering results of a composite of falling ice crystals spanning sixteen minutes. The resulting phase function is displayed in Fig. 7 for comparison with VPSEM-derived results. The SGBL result exhibits near-complete extinction of the 120° minimum and of the 46° halo, but substantial retention of the 22° halo. SGBL argue that these features constitute evidence of roughening in the range $\sigma_W = 0.1$ to 0.25, i.e., substantial roughening. An alternative hypothesis prompted by the present work is that the composite giving rise to this phase function contains a large component of trans-prismatic-roughened facets; this would allow for the simultaneous elimination of the 120° minimum and retention of the 22° halo. Unfortunately, the SGBL study did not allow for synchronization of the cloud particle imaging and nephelometry datasets that might resolve these competing hypotheses. In the same study, SGBL retrieved Weibull shape parameter (η_W) values in the range 0.73-0.77. This result is consistent with our finding that η_W is smaller than unity, although it predicts a somewhat

more peaked probability density function compared to our results. In separate work, however, [*Baran and Labonnote*, 2007] have shown that satellite data is best simulated using Weibull distribution parameters of η_W =0.85 and σ_W =0.4, values that align more closely with the present results.

A third consideration concerns whether the resilience of the 22° halo to VPSEM-derived roughening described here is a secure prediction, given the fact that geometric optics has been found to overestimate the intensity of the halo in other contexts [*Hesse and Ulanowski*, 2003]. At present this must be regarded as an open question, pending more sophisticated calculations.

A fourth set of considerations derives from advances in our understanding of the ice-vapor interface at the atomistic level. Recent molecular dynamics (MD) studies of the ice-vapor interface have indicated significant anisotropy in self-diffusion at the prismatic ice-vapor interface at temperatures below a threshold of -40° to -50°C; above this threshold, self-diffusion becomes isotropic [*Gladich et al.*, 2011]. A principle emerging from studies of nucleation and growth on anisotropic crystalline surfaces is that anisotropic diffusion leads *generically* to elongated mesoscopic islands like the trans-prismatic corrugations observed here [*Brune*, 1998]. These considerations point to the possibility of a mesoscopic rough-to-smooth transition in the -40° to -50°C temperature range. Such an inference must be considered very speculative, however, until the mechanisms by which mesoscopic roughness occurs are much more clearly understood.

6. Conclusions

We have defined a roughness metric, $<r>$, for mesoscopically rough ice facets, and presented methods for inferring its value from variable pressure scanning electron micrographs. The methods rely on the anisotropic morphology of roughening in the prismatic plane, in which nearly all the variation in surface height occurs in the direction of the main symmetry axis of hexagonal-habit ice prisms. The advantage of using this metric over more familiar scale parameters of roughness is that it is applicable to observed single-valued surface height functions, as well as to analytical roughness representations (e.g., random-tilt algorithms). Relationships between $<r>$ and these more familiar scale parameters are also provided. Prismatic surfaces of four ice crystals grown between -45 and -30°C are found to have $<r>=0.04$-0.1, a range that corresponds to random-tilt scale parameters $t_M \approx \sigma_{CM} \approx 0.3$-$0.5$. For three of the crystals presented here, probability densities of r are found to be consistent with Weibull shape parameters smaller than unity, in agreement with *in situ* observations of natural ice crystals at South Pole Station; a fourth exhibits too little probability at low r-values. Shortwave ray-tracing calculations of model hexagonal polyhedra with surface morphologies derived from these observations indicate substantial retention of the well-known 22° halo, despite a large (4-6%) reduction in the asymmetry parameter. We argue on theoretical grounds that this signature is a generic outcome of the trans-prismatic symmetry of the roughening, which we speculate originates in the anisotropic surface self-diffusivity of these facets.

The methods described here, in combination with cryoscopic SEM instrumentation having higher resolution [*Amaral et al.*, 2012], higher operating pressure capability [*Mathieu et al.*, 2007], or broader temperature range, offer the possibility of resolving outstanding uncertainties regarding the relationship between SEM-produced roughening observed here and roughening that occurs in atmospheric ice. Moreover, the present work argues for deployment of instruments that measure scattered intensity over a larger scattering angle domain, and for synchronized cloud particle imaging and nephelometry capability in future *in situ* measurements. Finally, we should emphasize that the ray-tracing calculations presented here are valid only in the geometric optics light-scattering regime, which require that the wavelength of light be small compared to the scale of the roughening. Characterization of the effects of roughening of the kind presented here on infrared scattering is a matter for future research.

Acknowledgements

SN, BL, AL, and MB gratefully acknowledge support from the University of Puget Sound. SN acknowledges helpful conversations with David Anick. All authors gratefully acknowledge three anonymous reviewers, whose comments greatly improved the manuscript.

References

Amaral, M., A. L. Miller, and N. B. Magee (2012), A13I-0301: Environmental Scanning Electron Microscopy of Ice Crystal Nucleation and Growth - AGU Fall Meeting 2012, San Fransisco. [online] Available from: http://fallmeeting.agu.org/2012/eposters/eposter/a13i-0301/ (Accessed 26 December 2012)

Bacon, N. J., M. B. Baker, and B. D. Swanson (2003), Initial stages in the morphological evolution of vapour-grown ice crystals: A laboratory investigation, *Quarterly Journal of the Royal Meteorological Society*, *129*(591), 1903–1927, doi:10.1256/qj.02.04.

Bailey, M., and J. Hallett (2004), Growth rates and habits of ice crystals between-20 and-70 C, *Journal of the atmospheric sciences*, *61*(5), 514–544.

Bailey, M. P., and J. Hallett (2009), A comprehensive habit diagram for atmospheric ice crystals: Confirmation from the laboratory, AIRS II, and other field studies, *Journal of the Atmospheric Sciences*, *66*(9), 2888–2899.

Baran, A. J. (2009), A review of the light scattering properties of cirrus, *Journal of Quantitative Spectroscopy and Radiative Transfer*, *110*(14-16), 1239–1260.

Baran, A. J. (2012), From the single-scattering properties of ice crystals to climate prediction: A way forward, *Atmospheric Research*, *112*, 45–69, doi:10.1016/j.atmosres.2012.04.010.

Baran, A. J., and L.-C. Labonnote (2007), A self-consistent scattering model for cirrus. I: The solar region, *Quarterly Journal of the Royal Meteorological Society*, *133*(629), 1899–1912, doi:10.1002/qj.164.

Baran, A. J., P. Yang, and S. Havemann (2001), Calculation of the Single-Scattering Properties of Randomly Oriented Hexagonal Ice Columns: A Comparison of the< i> T</i>-Matrix and the Finite-Difference Time-Domain Methods, *Applied Optics*, *40*(24), 4376–4386.

Baum, B. A., A. J. Heymsfield, P. Yang, and S. T. Bedka (2005a), Bulk scattering properties for the remote sensing of ice clouds. Part I: Microphysical data and models, *Journal of applied meteorology*, *44*(12), 1885–1895.

Baum, B. A., P. Yang, A. J. Heymsfield, S. Platnick, M. D. King, Y. X. Hu, and S. T. Bedka (2005b), Bulk scattering properties for the remote sensing of ice clouds. Part II: Narrowband models, *Journal of applied meteorology*, *44*(12), 1896–1911.

Bourdages, L., T. J. Duck, G. Lesins, J. R. Drummond, and E. W. Eloranta (2009), Physical properties of High Arctic tropospheric particles during winter, *Atmos. Chem. Phys*, *9*, 6881–6897.

Brune, H. (1998), Microscopic view of epitaxial metal growth: nucleation and aggregation, *Surface science reports*, *31*(4), 125–229.

Cox, C., and W. Munk (1954), Measurement of the roughness of the sea surface from photographs of the sun's glitter, *J Opt Soc Amer*, *44*. [online] Available from: http://userpages.umbc.edu/~martins/phys650/Cox%20and%20Munk%20Glint%20paper.pdf (Accessed 22 June 2012)

Cox, S. K. (1971), Cirrus Clouds and the Climate., *Journal of Atmospheric Sciences*, *28*, 1513–1514.

Crane, K. G., and R. G. Barry (1984), The influence of clouds on climate with a focus on high latitude interactions, *Journal of Climatology*, *4*(1), 71–93, doi:10.1002/joc.3370040106.

Cross, J. D. (1969), Scanning electron microscopy of evaporating ice., *Science (New York, NY)*, *164*(3876), 174.

Davy, J. G., and D. Branton (1970), Subliming ice surfaces: Freeze-etch electron microscopy, *Science*, *168*, 1216–1218.

Dodson, B. (2006), *The Weibull analysis handbook*, American Society for Qualit. [online] Available from: http://books.google.com/books?hl=en&lr=&id=5GzgBpdJkHwC&oi=fnd&pg=PR11&dq=+weibull+analysis+dodson&ots=T2D7LsE5ii&sig=-JSMcvteAx2UAwljZquskiXeAyY (Accessed 9 December 2012)

Edwards, J. M., S. Havemann, J.-C. Thelen, and A. J. Baran (2007), A new parametrization for the radiative properties of ice crystals: Comparison with existing schemes and impact in a GCM, *Atmospheric Research*, *83*(1), 19–35, doi:10.1016/j.atmosres.2006.03.002.

Garrett, T. J. (2008), Observational quantification of the optical properties of cirrus cloud, in *Light Scattering Reviews 3*, edited by A. A. Kokhanovsky, pp. 3–26, Springer Berlin Heidelberg. [online] Available from: http://www.springerlink.com/content/jt27170731542766/abstract/ (Accessed 16 June 2012)

Gayet, J. F., O. Crépel, J. F. Fournol, and S. Oshchepkov (1997), A new airborne Polar Nephelometer for the measurements of optical and microphysical cloud properties. Part I: Theoretical design, in *Annales Geophysicae*, vol. 15, pp. 451–459.

Gladich, I., W. Pfalzgraff, O. Maršálek, P. Jungwirth, M. Roeselová, and S. Neshyba (2011), Arrhenius analysis of anisotropic surface self-diffusion on the prismatic facet of ice, *Phys. Chem. Chem. Phys.*, *13*(44), 19960–19969.

Gonda, T., Y. Matsuura, and T. Sei (1994), In situ observation of vapor-grown ice crystals by laser two-beam interferometry, *Journal of Crystal Growth*, *142*(1–2), 171–176, doi:10.1016/0022-0248(94)90285-2.

Harrington, J. Y., D. Lamb, and R. Carver (2009), Parameterization of surface kinetic effects for bulk microphysical models: Influences on simulated cirrus dynamics and structure, *Journal of Geophysical Research*, *114*(D6), D06212.

Hesse, E., and Z. Ulanowski (2003), Scattering from long prisms computed using ray tracing combined with diffraction on facets, *Journal of Quantitative Spectroscopy and Radiative Transfer*, *79–80*, 721–732, doi:10.1016/S0022-4073(02)00317-5.

Heymsfield, A. J., and L. J. Donner (1990), A scheme for parameterizing ice-cloud water content in general circulation models, *Journal of the atmospheric sciences*, *47*(15), 1865–1877.

Heymsfield, A. J., and C. M. R. Platt (1984), A Parameterization of the Particle Size Spectrum of Ice Clouds in Terms of the Ambient Temperature and the ice Water Content, *Journal of Atmospheric Sciences*, *41*(5), 846–855.

Heymsfield, A. J., C. Schmitt, and A. Bansemer (2006), Measurements in low latitude high altitude cirrus, in *12th Conference on Cloud Physics*, pp. 10–14.

Hobbs, P. V., and W. D. Scott (1965), Step-growth on single crystals of ice, *Philosophical Magazine*, *11*(113), 1083–1086.

Jeong, H.-C., and E. D. Williams (1999), Steps on surfaces: experiment and theory, *Surface Science Reports*, *34*(6–8), 171–294, doi:10.1016/S0167-5729(98)00010-7.

Lynch, D. K. (2002), *Cirrus*, Oxford University Press.

Macke, A. (1993), Scattering of light by polyhedral ice crystals, *Applied optics*, *32*(15), 2780–2788.

Macke, A., J. Mueller, and E. Raschke (1996), Single scattering properties of atmospheric ice crystals, *Journal of the Atmospheric Sciences*, *53*(19), 2813–2825.

Macke, A., P. N. Francis, G. M. McFarquhar, and S. Kinne (1998), The role of ice particle shapes and size distributions in the single scattering properties of cirrus clouds, *Journal of the atmospheric sciences*, *55*(17), 2874–2883.

Mathieu, C., L. Khouchaf, and A. Kadoun (2007), Exploring the high pressure SEM, in *Modern Research and Educational Topics in Microscopy*, edited by A. Méndez-Vilas and J. Diaz, pp. 779–786, FORMATEX.

McFarlane, S. A., and K. F. Evans (2004), Clouds and shortwave fluxes at Nauru. Part II: Shortwave flux closure, *J. Atmos. Sci.*, *61*, 2602–2615.

Nelson, J. T., and M. B. Baker (1996), New theoretical framework for studies of vapor growth and sublimation of small ice crystals in the atmosphere, *Journal of Geophysical Research-All Sections-*, *101*, 7033–7047.

Pfalzgraff, W. C., R. M. Hulscher, and S. P. Neshyba (2009), Scanning electron microscopy and molecular dynamics of surfaces of growing and ablating hexagonal ice crystals, *Atmospheric Chemistry and Physics Discussions*, *9*(5), 20739–20763, doi:10.5194/acpd-9-20739-2009.

Pfalzgraff, W. C., R. M. Hulscher, and S. P. Neshyba (2010), Scanning electron microscopy and molecular dynamics of surfaces of growing and ablating hexagonal ice crystals, *Atmos. Chem. Phys*, *10*, 2927–2935.

Sazaki, G., S. Zepeda, S. Nakatsubo, E. Yokoyama, and Y. Furukawa (2010), Elementary steps at the surface of ice crystals visualized by advanced optical microscopy, *Proceedings of the National Academy of Sciences*, *107*(46), 19702–19707.

Schmitt, C. G., and A. J. Heymsfield (2007), On the occurrence of hollow bullet rosette-and column-shaped ice crystals in midlatitude cirrus, *Journal of the Atmospheric Sciences*, *64*(12), 4514–4519.

Shcherbakov, V., J. F. Gayet, O. Jourdan, J. Ström, and A. Minikin (2006a), Light scattering by single ice crystals of cirrus clouds, *Geophysical research letters*, *33*(15), L15809.

Shcherbakov, V., J. F. Gayet, B. Baker, and P. Lawson (2006b), Light scattering by single natural ice crystals, *Journal of the atmospheric sciences*, *63*(5), 1513–1525.

Stephens, G., S. Tsay, P. W. Stackhouse, and P. J. Flatau (1990), The relevance of the microphysical and radiative properties of cirrus clouds to climate and climatic feedback, *Journal of the atmospheric sciences*, *47*(14), 1742–1753.

Ulanowski, Z., E. Hesse, P. H. Kaye, and A. J. Baran (2006), Light scattering by complex ice-analogue crystals, *Journal of Quantitative Spectroscopy and Radiative Transfer*, *100*(1–3), 382–392, doi:10.1016/j.jqsrt.2005.11.052.

Walden, V. P., S. G. Warren, and E. Tuttle (2003), Atmospheric ice crystals over the Antarctic Plateau in winter, *Journal of Applied Meteorology*, *42*(10), 1391–1405.

Warren, S. G., and R. E. Brandt (2008), Optical constants of ice from the ultraviolet to the microwave: A revised compilation, *Journal of Geophysical Research*, *113*(D14), D14220.

Xie, Y. (2012), The effect of ice crystal surface roughness on the retrieval of ice cloud microphysical and optical properties, Texas A&M University, 30 November. [online] Available from: http://repositories.tdl.org/tdl-ir/handle/1969.1/5970 (Accessed 7 December 2012)

Yang, P., and K. N. Liou (1998), Single-scattering properties of complex ice crystals in terrestrial atmosphere, *Beitrage zur Physik der Atmosphare-Contributions to Atmospheric Physics*, *71*(2), 223–248.

Yang, P., H. Wei, H. L. Huang, B. A. Baum, Y. X. Hu, G. W. Kattawar, M. I. Mishchenko, and Q. Fu (2005), Scattering and absorption property database for nonspherical ice particles in the near-through far-infrared spectral region, *Applied optics*, *44*(26), 5512–5523.

Yang, P., G. W. Kattawar, G. Hong, P. Minnis, and Y. Hu (2008a), Uncertainties Associated With the Surface Texture of Ice Particles in Satellite-Based Retrieval of Cirrus Clouds—Part I: Single-Scattering Properties of Ice Crystals With Surface Roughness, *Geoscience and Remote Sensing, IEEE Transactions on*, *46*(7), 1940–1947.

Yang, P., G. Hong, G. W. Kattawar, P. Minnis, and Y. Hu (2008b), Uncertainties Associated With the Surface Texture of Ice Particles in Satellite-Based Retrieval of Cirrus Clouds: Part II—Effect of Particle Surface Roughness on Retrieved Cloud Optical Thickness and Effective Particle Size, *Geoscience and Remote Sensing, IEEE Transactions on*, *46*(7), 1948–1957.

Figure Captions

Figure 1. (a) Illustration of a surface normal vector, $\vec{n}$, the viewing vector, $\vec{d}$, and the angle between them, $\phi(z)$, for a sinusoidal surface height function. The sinusoidal characteristic angle, δ_c, is the maximum angle subtended by a sinusoidal surface height function with respect to the reference plane. (b) The surface normal roughness parameter, r, for this height function (see Eq. (4)).

Figure 2. Roughness parameters as a function of the mean surface normal roughness, $< r >$. (a) the approximate characteristic angle, δ_c°, of a sinusoidal surface height function; (b) the exact characteristic angle, δ_c (both scaled by 2/π; see Eqs. (6-8)); (c) the Macke distortion parameter, t_M; (d) the Cox-Munk scale parameter, σ_{CM} (which equals σ_W when $\eta_W = 1$), and (e) the Weibull scale parameter, σ_W, when $\eta_W = 0.75$. Vertical bars indicate <r> values for Crystals I-IV (see Figs. 3-4).

Figure 3. Series of VPSEM micrographs depicting prismatic facets of a hexagonal prism undergoing a growth-ablation cycle. The z-axis is collinear with the main symmetry axis (c-axis) of the prism. The bright diagonal line appearing in each micrograph marks a boundary between two prismatic facets, one (upper right of each panel) having a surface normal parallel to the viewing vector, the other (lower left) having a surface normal inclined at 60° from the viewing vector. (A-B) ice crystals growing at -45°C; the time from crystal detection to B was about three minutes. (C-E) ice crystals ablating as a result of raising the Peltier cooler temperature to -32°C, over the course of two minutes. (F-H)

ice crystals growing as a result of restoring the Peltier cooler temperature to -45°C, over the course of seven minutes.

Figure 4. Morphological properties of rough prismatic facets. Left column: VPSEM micrographs of ice crystals with prismatic roughening. Middle column: Surface height and the surface normal roughness variable derived from these micrographs (c.f. Eq. 4). Right column: Polyhedra with VPSEM-derived roughness, all with an aspect ratio of four.

Figure 5. Ensemble of profiles of electron backscattered intensity, *I(x)*, taken from region R of Crystal III in Fig. 4; each profile corresponds to a different value of z (See Fig. 3A for definitions of coordinates x and z). Peaks define $x_{boundary}(z)$, which coincide with the bright prismatic facet boundary appearing in the third row of Fig. 4.

Figure 6. Normalized probability density functions of the surface normal roughness variable. All random-tilt parameterizations are consistent with <r>=0.051 to match Crystal I.

Figure 7. Orientation-averaged phase functions of hexagonal polyhedra with varying roughness representations, all having an aspect ratio of four. Gray indicates individual VPSEM-derived crystals I-IV, the black solid line represents their mean. Curves labeled "Smooth" and "URT" pertain to an unroughened and URT-roughened crystals of the same dimensions as Crystal I. The SGBL phase function [*Shcherbakov et al.*, 2006b], for

which normalization is not available, has been scaled to match that of VPSEM-derived and URT roughened results at a scattering angle of 45°. (a) Scattering phase function; (b) Linear depolarization ratios, as defined by [*Baran*, 2009].

Figure 8. Asymmetry parameters of roughened hexagonal ice columns from ray tracing. Uncircled markers, in red, are URT-roughened results. The reduction in asymmetry parameter for polyhedra with VPSEM-derived roughness, with respect to smooth-surface counterparts, is 4-6%.

Figure 9. Photographs of atmospheric ice recorded at ground level. (a) A bullet cluster of tapered hexagonal ice prisms photographed on 21 July 1992 at South Pole Station. This photograph is a high-resolution version of Fig. 2(c) of [*Walden et al.*, 2003]. (b) Aggregate and bullet clusters photographed on 25 February 2011 at Summit, Greenland. (c) Crystal photographed on 27 June 2010 at Summit, Greenland. Photographs provided by [*Walden*, personal communication].

Table 1. Measured and modeled properties of rough hexagonal columns. Polyhedra constructed for ray-tracing calculations have been assigned an aspect ratio of four.

	VPSEM notes	<r>	t_M	σ_{CM}	δ_c	# planes	c (μm)
I	Initially grown at $-45^{\circ}C$, then raised to $-32^{\circ}C$ to induce ablation roughening	0.051	0.36	0.34	25°	542	259
II	Growth-only roughening at $-45^{\circ}C$	0.102	0.51	0.52	36°	632	236
III	Growth-only roughening at $-45^{\circ}C$	0.038	0.31	0.29	22°	836	101
IV	Growth-only roughening at $-45^{\circ}C$	0.092	0.48	0.48	34°	626	89

Figure 1.

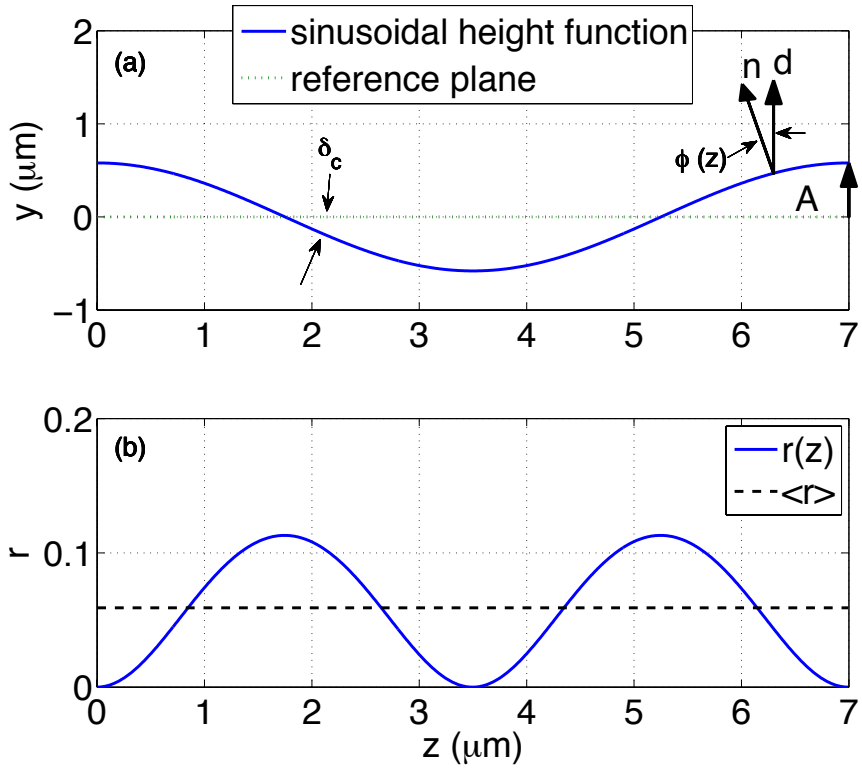
sinusoidal height function
reference plane
(a)
n d
δc
ϕ (z)
A
y (μm)
2
1
0
−1
0
1
2
3
4
5
6
7
(b)
r(z)
<r>
r
0.2
0.1
0
z (μm)

Figure 2.

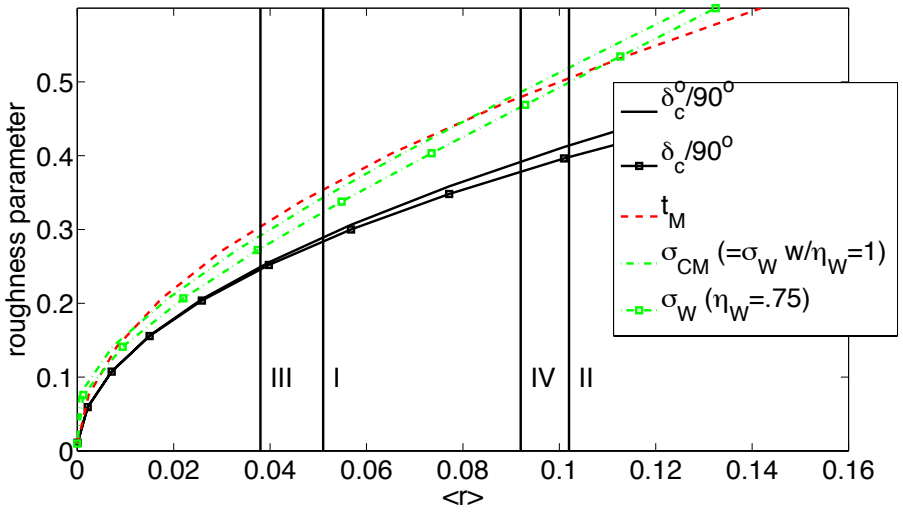
roughness parameter
<r>
0
0.1
0.2
0.3
0.4
0.5
0.02
0.04
0.06
0.08
0.12
0.14
0.16
III
I
IV
II
δc°/90°
δc/90°
tM
σCM (=σW w/ηW=1)
σW (ηW=.75)

Figure 3.

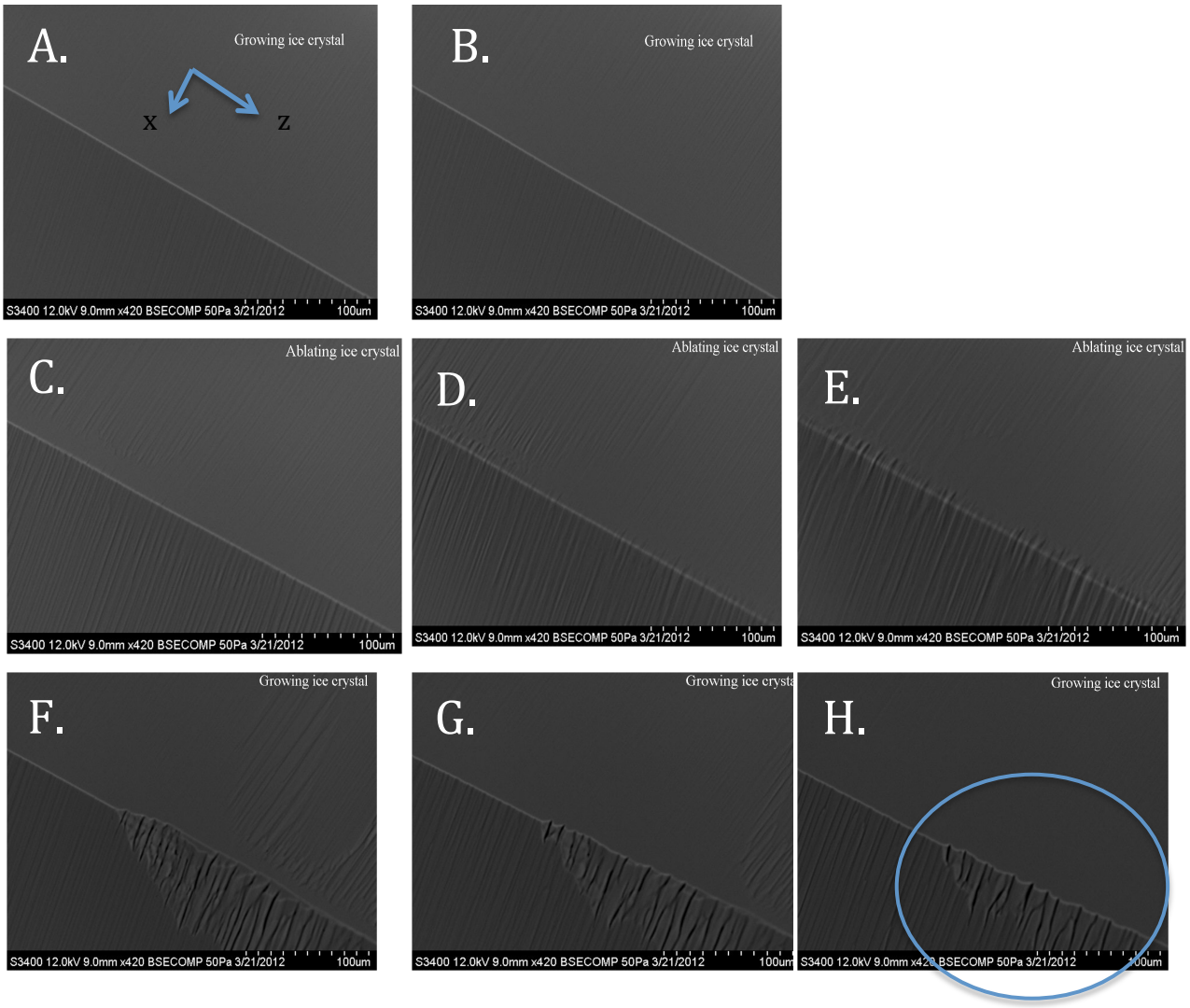
A.
Growing ice crystal
x
z
S3400 12.0kV 9.0mm x420 BSECOMP 50Pa 3/21/2012 100um
B.
Growing ice crystal
S3400 12.0kV 9.0mm x420 BSECOMP 50Pa 3/21/2012 100um
C.
Ablating ice crystal
S3400 12.0kV 9.0mm x420 BSECOMP 50Pa 3/21/2012 100um
D.
Ablating ice crystal
S3400 12.0kV 9.0mm x420 BSECOMP 50Pa 3/21/2012 100um
E.
Ablating ice crystal
S3400 12.0kV 9.0mm x420 BSECOMP 50Pa 3/21/2012 100um
F.
Growing ice crystal
S3400 12.0kV 9.0mm x420 BSECOMP 50Pa 3/21/2012 100um
G.
Growing ice cryst
S3400 12.0kV 9.0mm x420 BSECOMP 50Pa 3/21/2012 100um
H.
Growing ice crystal
S3400 12.0kV 9.0mm x420 BSECOMP 50Pa 3/21/2012

Figure 4.

I ablating; deep

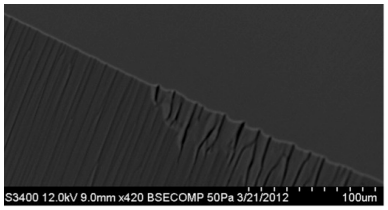

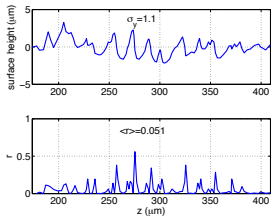

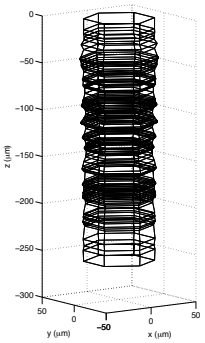

II growing; deep

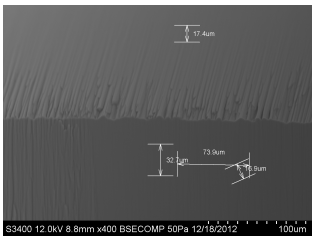

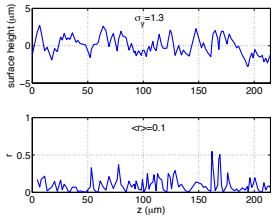

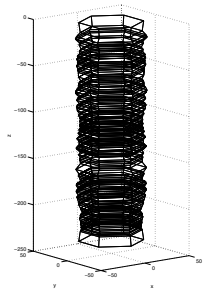

III growing; shallow

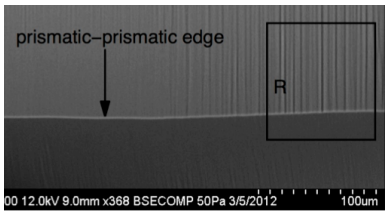

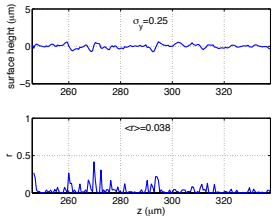

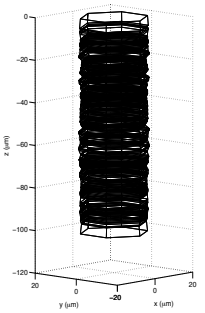

IV growing; shallow

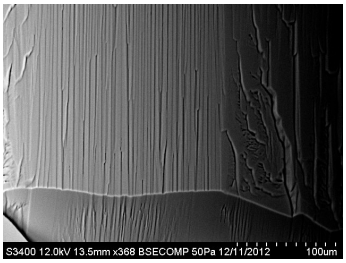

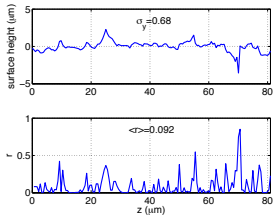

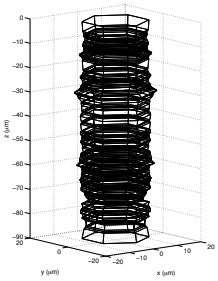

Figure 5.

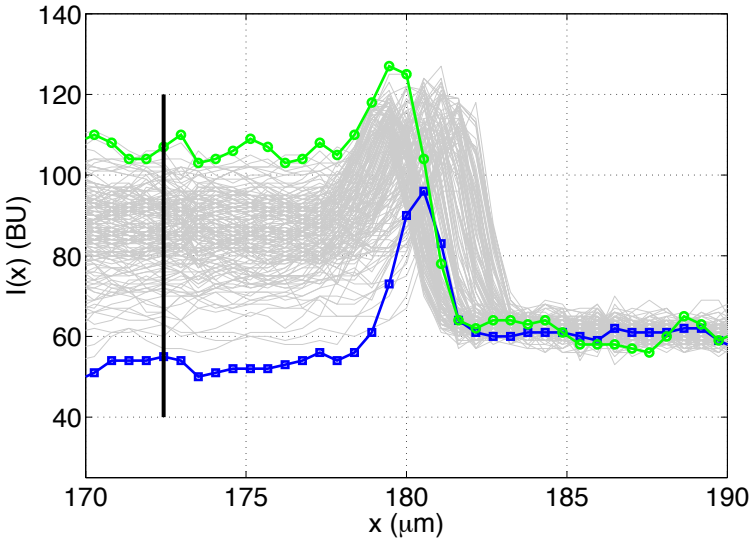

Figure 6.

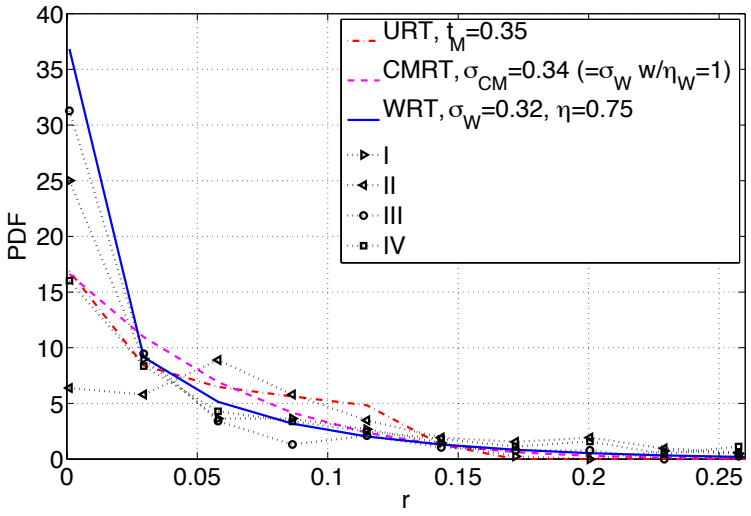
URT, t_M=0.35
CMRT, σ_{CM}=0.34 (=σ_W w/η_W=1)
WRT, σ_W=0.32, η=0.75
I
II
III
IV
PDF
r
0
5
10
15
20
25
30
35
40
0
0.05
0.1
0.15
0.2
0.25

Figure 7.

(a)

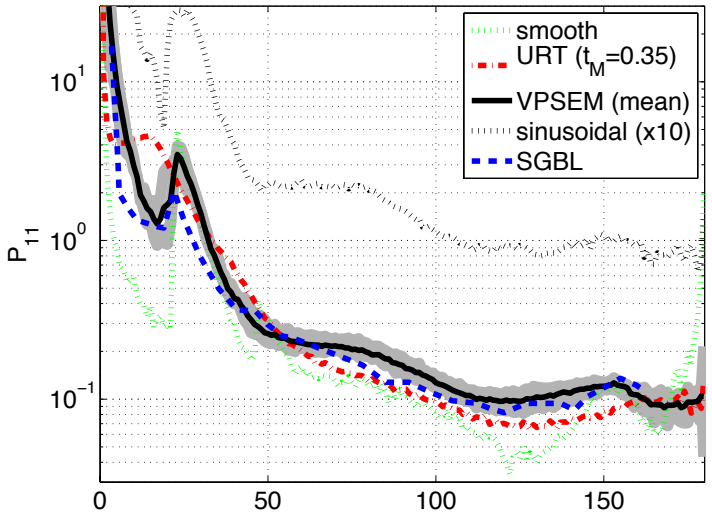
smooth
URT (t_M=0.35)
VPSEM (mean)
sinusoidal (x10)
SGBL
P_{11}
10^1
10^0
10^{-1}
0
50
100
150

(b)

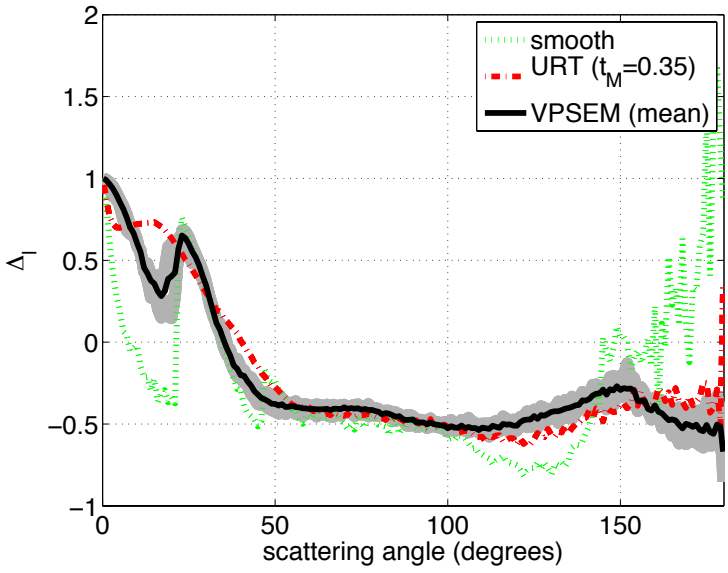
smooth
URT (t_M=0.35)
VPSEM (mean)
Δ_I
2
1.5
1
0.5
0
−0.5
−1
0
50
100
150
scattering angle (degrees)

(b)

Figure 8.

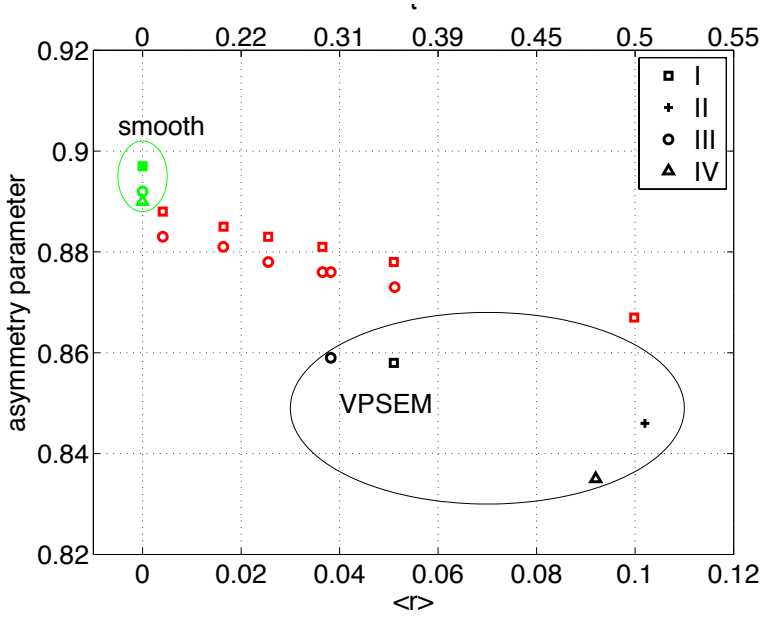
0
0.22
0.31
0.39
0.45
0.5
0.55
0.92
0.9
0.88
0.86
0.84
0.82
asymmetry parameter
smooth
VPSEM
I
II
III
IV
0
0.02
0.04
0.06
0.08
0.1
0.12
<r>

Figure 9.